PAPER AAS 91-515

THE ROLE OF PREDICTED SOLAR ACTIVITY IN TOPEX/POSEIDON ORBIT MAINTENANCE MANEUVER DESIGN

R. B. Frauenholz
B. E. Shapiro
Jet Propulsion Laboratory
California Institute of Technology
Pasadena, California

AAS/AIAA Astrodynamics Specialist Conference

Durango, Colorado August 19-22, 1991
AAS Publications Office, P.O. Box 28130, San Diego CA 92128

This paper is a declared work of the U. S. Government and is not subject to copyright protection in the United States.

THE ROLE OF PREDICTED SOLAR ACTIVITY IN TOPEX/POSEIDON ORBIT MAINTENANCE MANEUVER DESIGN*

Raymond B. Frauenholz† and Bruce E. Shapiro‡

Jet Propulsion Laboratory, California Institute of Technology, Pasadena, Ca.

Following launch in June 1992, the TOPEX/POSEIDON satellite will be placed in a near–circular frozen orbit at an altitude of ~1336 km. Orbit maintenance maneuvers are planned to assure all nodes of the 127–orbit 10–day repeat ground track remain within a 2–km equatorial longitude bandwidth. Orbit determination, maneuver execution, and atmospheric drag prediction errors limit overall targeting performance. This paper focuses on the effects of drag modelling errors, with primary emphasis on the role of SESC solar activity predictions, especially the 27–day outlook of the 10.7–cm solar flux and geomagnetic index used by a simplified version of the Jacchia–Roberts density model developed for this TOPEX/POSEIDON application. For data evaluated from 1983–90, the SESC outlook performed better than a simpler persistence strategy, especially during the first 7–10 days. A targeting example illustrates the use of ground track biasing to compensate for expected orbit predictions errors, emphasizing the role of solar activity prediction errors.

INTRODUCTION

The Ocean Topography Experiment (TOPEX/POSEIDON) satellite is currently scheduled to be launched in June 1992 by an Ariane from French Guiana and begin a three–year global study of the Earth's oceans utilizing a dual–frequency radar altimeter and a solid–state altimeter. Ultimately, ocean surface height is to be measured to an accuracy of 13 cm (3σ) using satellite altimetry and precision orbit determination[1] (POD) based on laser tracking data. These science studies will be conducted from a near–circular frozen orbit at an altitude of ~1336 km and an inclination of ~66 deg. The current baseline operational orbit provides a 10–day repeat of the satellite ground track during which it will overfly single NASA and CNES ground verification sites.

To satisfy these mission objectives requires precise control of the satellite ground track and minimum interference from orbit maintenance maneuvers. During the first six months, 95% of the planned verification site overflights must be controlled within ±1 km. Supporting maneuvers are constrained to occur over land between pre–determined 10–day ground track repeat cycles to avoid possible interference with on–going altimetry and POD processing, while assuring with 95% probability that the maneuver spacing is at least 30 days. After six months, the ground tracks are to be controlled within a 2–km equatorial bandwidth; maneuvers are to be "as infrequent as practical," and spaced to occur over land between 10–day repeat cycles.

Earlier work by Bhat[2] describes the maneuver strategies necessary to provide the required orbit control within the frame–work of expected navigation system errors, including orbit determination, maneuver execution, and atmospheric drag modelling uncertainties. The effect of geopotential modelling errors on the satellite ground track are expected to be minimal as a result of extensive pre–launch model development[3] and post–launch improvements planned during the first six months. Consequently, atmospheric drag prediction errors

* The research described in this paper was carried out by the Jet Propulsion Laboratory, California Institute of Technology, under contract with the National Aeronautics and Space Administration.

† Technical Manager, Member AIAA

‡ Member Technical Staff, Member AIAA

are expected to limit overall targeting accuracy, particularly early in the mission during the period of highest solar activity.

This paper focuses on the effects of drag modelling errors on the maneuver design, with special emphasis on the role of solar activity predictions in this process. Solar activity prediction errors are determined and expressed in terms of ground track errors. A targeting example illustrates the use of ground track biasing to compensate for expected solar activity predictions errors.

ORBIT PROPAGATION MODEL

Preliminary maneuver design determines the approximate time and magnitude of orbit corrections necessary to maintain the satellite ground track within required limits. This process requires a rapid and efficient orbit propagation model that considers all perturbations that cause significant variations in the satellite ground track. Bhat[2] has developed such a model based on mean orbital element propagation. Reference mean elements determined by Vincent[4] define a reference ground track with a 10–day repeat cycle that overflys the NASA and CNES verification sites in the presence of a 17×17 gravity field. Guinn[5] has developed a method of converting between mean and osculating elements that includes the effects of zonal and tesseral harmonics, second–order J_2, and third–body perturbations. Bhat's dynamic model accomodates gravity terms up to 29×29, atmospheric drag, and luni–solar gravitational perturbations. The effects of solar radiation pressure were omitted since the resulting ground track variations are significantly smaller than those caused by other perturbations; their omission does not alter the character of the maneuver design.

Luni–solar gravity perturbs the ground track through periodic variations in the orbit inclination.[2] At the TOPEX/POSEIDON altitude these ground track perturbations are comparable to those induced by atmospheric drag; the direction depends on the ever–changing phasing of the sun and moon with respect to the satellite orbit orientation. Ultimately, the net effect of luni–solar gravity and atmospheric drag on the ground track must be dynamically modelled to maintain the required targeting accuracy.

ATMOSPHERIC DRAG MODELLING

Atmospheric drag causes a continuous decay in the orbit semi–major axis, resulting in an eastward drift in the satellite ground track. The decay rate[6] is a function of satellite physical parameters and the atmospheric density. Stringent ground track control requirements for TOPEX/POSEIDON impose the need for models of the satellite variable drag area and daily updates to solar activity parameters to reflect changes in atmospheric density.

Near–continuous yaw steering about the local nadir and solar panel pitching are utilized to maintain the dominant 28 m^2 solar panel area pointed toward the sun for power optimization. This attitude control strategy causes the true satellite drag area to continuously vary by as much as 4:1 during a single orbit period.[2] This Continuously Variable Area (CVA) is a rapid periodic function of orbit angle whose extrema are a slowly varying function of β', the angle between the orbit plane and the earth–sun line. The maximum CVA amplitude occurs when $\beta' = 0$, while the minimum drag area coincides with local maxima of β'. The period of β' variation is ~56 days. The use of a CVA model for orbit determination and prediction is computationally intense. Instead, required accuracies are achieved with an approximate Variable Mean Area (VMA)[2] model, which defines the mean area per orbit as a tabular function of β'.

Density models used for orbit propagation are usually derived empirically from actual flight data in terms of satellite drag estimates and daily observations of the $F_{10.7}$ solar flux, the planetary geomagnetic index K_p, and the 81–day centered mean solar flux $\overline{F_{10.7}}$. Unfortunately, candidate density models do not reflect flight data at the TOPEX/POSEIDON altitude, as none are presently available. Among the best available upper–atmosphere model candidates are the '64, '71, and '77 Jacchia models.[7,8,9] These models include contributions due to solar flux, geomagnetic activity, altitude, geographic position, and solar orientation, as well as an explicit time dependence, and require time–consuming numerical integrations to determine the density at each point in the orbit. For orbit determination and precise maneuver planning, Roberts[10] developed a more efficient analytic approximation to the Jacchia models. The Jacchia–Roberts (JR) model[11] provides explicit analytic expressions for evaluating the density $\rho(\vec{r}, T_\infty)$ as a function of satellite position $\vec{r}$ and exospheric temperature T_∞.

$$\rho = \rho_s(z) 10^{\Delta \log \rho} \tag{1}$$

The first factor in Eq. (1), $\rho_s(z)$, represents the sum total of the density contributions due to each constituent species. This factor was determined by Jacchia with a set of integrations of the diffusion and barometric equations from fixed boundary conditions at $z = 90$ km. The density strongly depends on thermal variations, which are themselves a function of the exospheric temperature $T_\infty = T_1 + \Delta T_\infty$ (in $^\circ K$), where

$$\begin{aligned} T_1 = T_c \Bigg\{ 1 + 0.03 \Bigg\{ & \sin^{2.2}\left(\frac{\phi+\delta}{2}\right) + \\ & \left[\cos^{2.2}\left(\frac{\phi-\delta}{2}\right) - \sin^{2.2}\left(\frac{\phi+\delta}{2}\right)\right] \times \\ & \cos^3\left[H - 37^\circ + 6^\circ \sin(H + 43^\circ)\right] \Bigg\} \Bigg\}, \\ T_c = 379^\circ + 3.24^\circ \overline{F}_{10.7} + 1.3^\circ \left[F_{10.7} - \overline{F}_{10.7}\right], \\ \Delta T_\infty = 28^\circ K_p + 0.03^\circ e^{K_p}, \end{aligned} \tag{2}$$

where ϕ is the geodetic latitude, δ is the solar declination, H is the solar hour angle, K_p is lagged by 6.7 hrs, $F_{10.7}$ is lagged by 24 hrs, and $\overline{F_{10.7}}$ is the 81–day average of $F_{10.7}$ *centered at the present time.* The second factor in Eq. (1) includes explicit corrections for geomagnetic activity, an explicit time–dependence with a semi–annual period, and a combined seasonal–latitudinal dependence:

$$\Delta \log \rho = (\Delta \log \rho)_{GA} + (\Delta \log \rho)_{SA} + (\Delta \log \rho)_{SL}. \tag{3}$$

The JR model approximates the true Jacchia model to within 7%. While providing a relatively quick analytic density evaluation, the JR model is still position and time dependent, and must be re–evaluated at each position in the orbit. This approach is reasonable for orbit determination, ephemeris generation, and precise maneuver planning, where a full numerical integration is required. However, for fast and efficient preliminary maneuver planning, a mean element propagation technique with a step size of at least one orbit is used. A simplified atmospheric model is utilized in this process.

The simplified density model (SDM) defines the average orbital density as

$$\rho_{SDM} = 10^{\overline{\log \rho}} \text{ kg/m}^3, \tag{4}$$

$$\text{where} \quad \overline{\log \rho} = P(\hat{T}_\infty) + a\cos(2\pi t + \phi_1) + b\cos(4\pi t + \phi_2). \tag{5}$$

$P(\hat{T}_\infty)$ is a quadratic function of the simplified exospheric temperature $\hat{T}_\infty$

$$\hat{T}_\infty = T_c + \Delta T_\infty. \tag{6}$$

$P(\hat{T}_\infty)$ is expressed in terms of a Chebyshev Basis with $n = 2$ as

$$\begin{aligned} u &= \frac{T_\infty - p_1}{p_2}, \\ z_n &= p_{n+3}, \\ z_{n-1} &= 2uz_n + p_{n+2}, \\ z_i &= 2uz_{i+1} - zi + 2 + p_{i+3}, \quad i = n-2, ..., 1 \\ P(T_\infty) &= uz_1 - z_2 + p_3. \end{aligned} \tag{7}$$

The coefficients p_i were determined from a least–squares fit of the average log density as a function of $\hat{T}_\infty$. Using data over a full 11–year solar cycle (1978–1988), 4018 orbital averages were computed at 24–hr intervals with the full JR model. Each orbital average was based upon ten equally spaced density calculations around a circular orbit at the TOPEX/POSEIDON altitude. The semi–annual and annual variations are modelled by least–squares sinusoidal fits to the density residuals after $P(\hat{T}_\infty)$ is evaluated. The time variable t is measured in years from 1 January at 00:00 GMT. The coefficients are:

$p_1 \simeq 1024.444$	$a \simeq 0.045$ kg/m^3
$p_2 \simeq 414.350$	$b \simeq -0.079$ kg/m^3
$p_3 \simeq -5.811$	$\phi_1 \simeq 6.105$ radians
$p_4 \simeq 0.721$	$\phi_2 \simeq 5.414$ radians
$p_5 \simeq 8.43 \times 10^{-5}$	

The error in the average density over the 11–year sample period, measured with respect to the full JR model, is 0.4%, with a spread of $\sigma \simeq 8.7\%$.

SOLAR ACTIVITY

As indicated earlier, the JR model defines atmospheric density in terms of exospheric temperature based on observations of the solar flux and geomagnetic activity (Eqs. 1,2). Solar flux is the rate of energy received per unit area per unit time. The $F_{10.7}$ solar flux provides an indirect measure of extreme ultraviolet (EUV) heating in the upper atmosphere at a radio wavelength of 10.7 cm, ranging in value from ~70 to over 300×10^{-22} watts/m^2/Hz. Geomagnetic activity is an indicator of joule heating induced by charged particles. There are several different geomagnetic indices, each having a specific use, or relating to a particular geographic region. For example, the AE index reflects conditions in the auroral zone, while the K and A indices are measures of geomagnetic activity at mid–latitudes. The index most frequently used for atmospheric density model development is A_p, the daily equivalent planetary amplitude index. This linear index has units of 2γ ($\gamma = 10^{-9}$ Tesla) with values ranging from 0 to 400, although values larger than 80 are quite rare. The A_p index was created from the older K_p index, which is a quasi–logarithmic number used to characterize

the level of worldwide geomagnetic activity at sub–auroral latitudes. The K_p index, ranging in value from 0 to 9, defines the daily average of eight individual K observations acquired once every three hours by a global network of magnetometers.

Use of the $F_{10.7}$ and K_p parameters limits density modelling accuracy. Marcos[12] indicates eight different models used with accelerometer data from four different satellites flown between 1964 and 1986 exhibited a relatively constant systematic density error of about 15% (1σ). Direct EUV monitoring from space would be a better and more timely indication of physical atmospheric heating than the $F_{10.7}$ solar flux, but this approach requires a network of suitably positioned satellites, a plan with obvious limitations. Also, the global array of magnetometers currently used to monitor A_p do not provide the desired uniform longitudinal coverage at a single geomagnetic latitude. Finally, and of major significance, much work has already been invested in density model development using available earth–based observations. Still, requirements remain for improved modelling accuracy. For example, Marcos, et al,[12] have recently initiated development of a new thermosphere–ionosphere model intended to improve density accuracies at all altitude regions between 90 and 1500 km.

One goal of this investigation is to better understand the capabilities and limitations imposed by use of the JR density model dependent on daily observations and predictions of $F_{10.7}$ and K_p. The basic behavior of these parameters is briefly described below, but more detailed descriptions are available in work by Nostrand,[13] Withbroe,[14] McCormac,[15] and Heckman,[16] all which also include comprehensive bibliographies of related literature.

Solar Flux and Geomagnetic Index Observations

The $F_{10.7}$ solar flux exhibits two periodic cycles of variation, both associated with the behavior of the sun. The primary periodic component relates to the 11–year solar cycle which directly reflects the level of sunspot activity. Figure 1 shows the *monthly* mean and moving average in $F_{10.7}$ since 1955, a period covering cycle 19 through the first half of current cycle 22. The declining phase of each cycle has been observed to be more active and longer–lasting than earlier phases, a behavior believed to be related to the reappearance of coronal holes as sunspot activity decreases.[16]

A higher frequency variation in $F_{10.7}$ occurs during a single solar disk rotation, a period of ~27 days. This variation reflects the daily behavior of active growth and decay patterns on the sun. Figure 2 shows an example of this variation from January 1990 through mid–June 1991, an interval spanning the peak of current cycle 22. While the recurring 27–day cycles are clearly visible, $F_{10.7}$ variations do not uniformly repeat for even a few cycles. The ability to predict this periodic variation directly affects orbit prediction accuracy.

Geomagnetic indices exhibit behavior related to the 11–year solar cycle, but also have more frequent semi–annual variations that are unrelated to the solar cycle. High geomagnetic activity is usually induced by flares near the solar maxima. However, the highest frequency of sustained high geomagnetic activity occurs during the declining phase of the solar cycle due to recurrent coronal hole disturbances. The period of greatest semi–annual variation occurs near each equinox when the magnetosphere is best–aligned for coupling with the interplanetary magnetic field. One good example is the great geomagnetic storm of 13 March 1989,[17] when A_p rocketed to ~250. Another more recent example of very high geomagnetic activity occurred on 5 June 1991 when an A_p of 150 was observed (Fig. 2).

The Space Environment Services Center (SESC) in Boulder, Co. is the primary source of solar activity measurements in the United States. The SESC is jointly operated by The National Oceanic and Atmospheric Administration (NOAA) and the U. S. Air Force Air Weather Service (USAWS). The SESC distributes data collected by its own sensors and by cooperating agencies throughout the world. The adopted standard for the $F_{10.7}$ solar flux is the daily observation at 1700Z acquired in Ottawa by the Canadian National Research Council. The SESC also provides daily observations of both A_p and K_p geomagnetic indices. The SESC makes these *uncorrected* data electronically accessible and also in weekly issues of the *Preliminary Report and Forecast of Solar Geophysical Data (PRF)*. The SESC also publishes other data, including a monthly summary report.

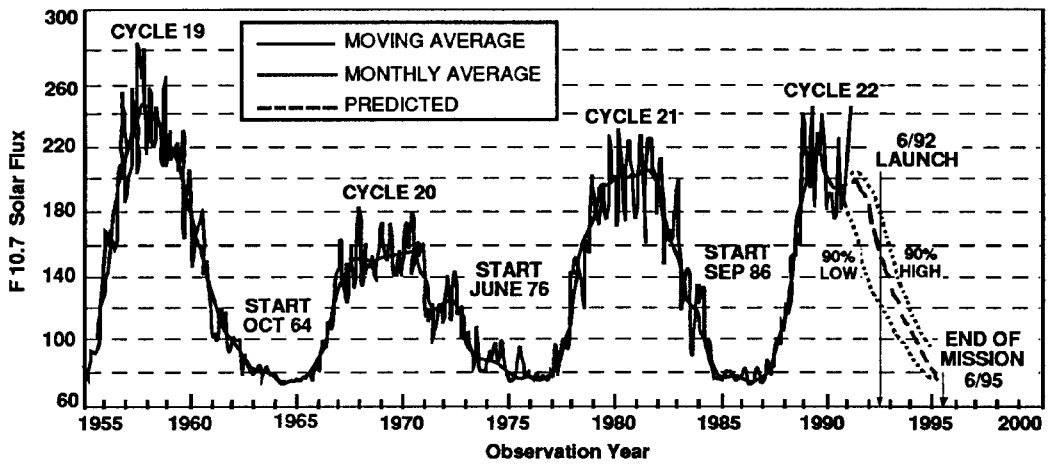

Fig. 1. Long–Term Variations in the Mean $F_{10.7}$ Solar Flux (Cycles 19–22).

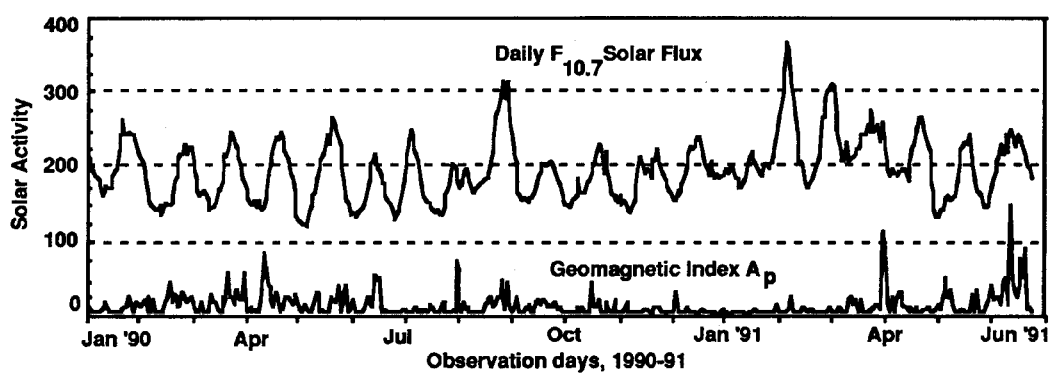

Fig. 2. Recent Daily Variations in the $F_{10.7}$ Solar Flux and Geomagnetic Index A_p.

Within a few months after acquiring *uncorrected* observations, the SESC issues corrected values normalized to a distance of 1 AU, with known instrumentation and processing errors removed. Normalized values are convenient for many solar physics investigations, but are inappropriate for orbit propagation applications. The use of corrected values with normalization removed would improve overall measurement quality, but these data are not available for timely use in most satellite operations activities.

Figure 3(a) shows the variations in the *uncorrected* daily $F_{10.7}$ and A_p observations from mid–April 1983 to mid–June 1991. This period has been selected for study because in April 1983 the SESC first began to archive the 27–day outlook for $F_{10.7}$ and A_p in weekly *PRFs*. While this database covers less than one solar cycle, it does include a cycle decline period similar to that expected during the TOPEX/POSEIDON mission (see Fig. 1). Figs. 3(b,c) show the annual mean and standard deviation of the observed $F_{10.7}$ and K_p from 1983–91. As expected, K_p has a larger mean and greater variability during the declining years of the solar cycle.

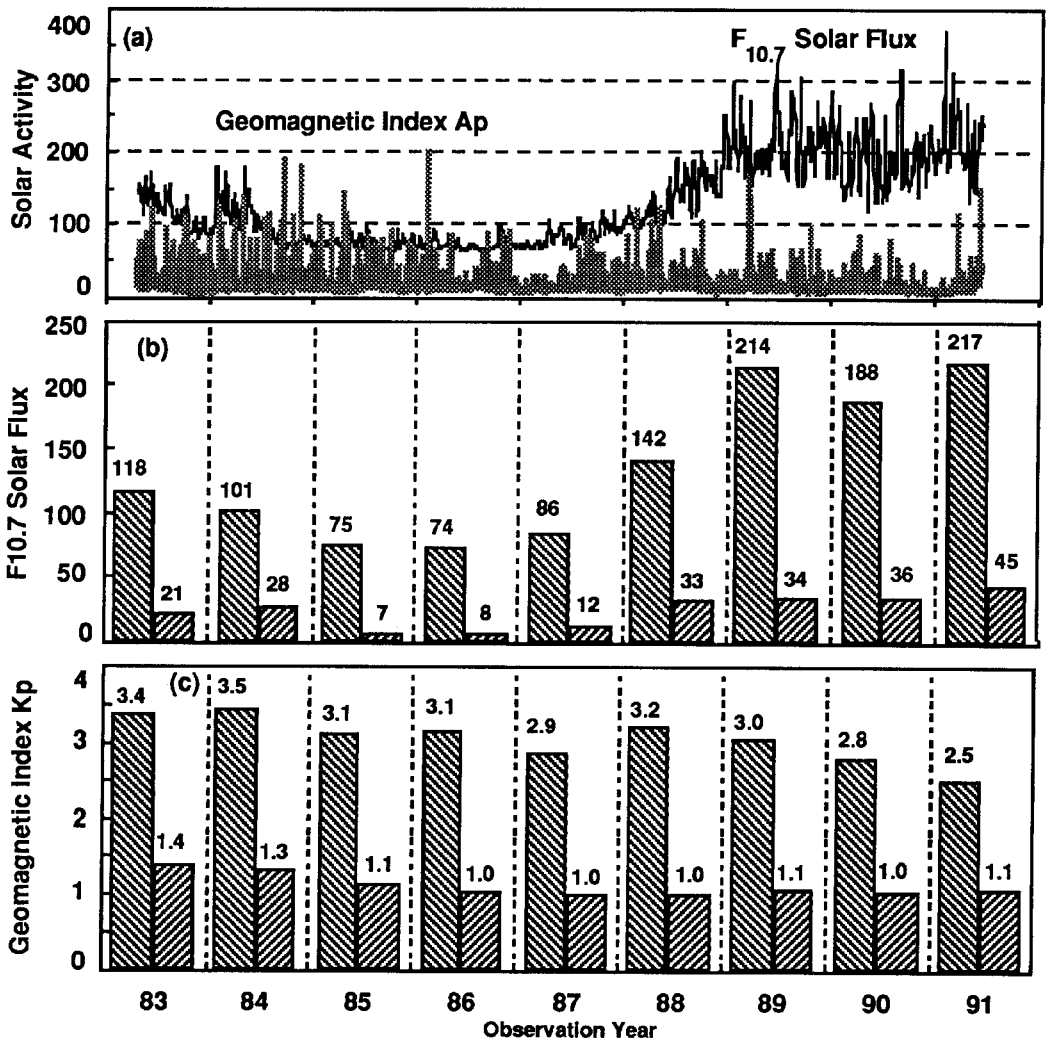

Fig. 3. Daily Solar Activity Observations (April 1983 to mid–June 1991):
(a) Daily $F_{10.7}$ Solar Flux and Geomagnetic Index A_p,
(b) Annual Mean and Standard Deviation of Daily $F_{10.7}$ Solar Flux,
(c) Annual Mean and Standard Deviation of Daily Geomagnetic Index K_p.

Solar Flux Predictions

The prediction accuracies of $F_{10.7}$ and K_p have a major influence on orbit propagation problems, especially when constrained by stringent control requirements. Since previous flight data are not available at the TOPEX/POSEIDON flight altitude to calibrate the JR density model, in–flight estimates of a drag scale factor are expected to be necessary to help meet these control requirements. Drag modelling accuracy then becomes limited by $F_{10.7}$ and K_p prediction accuracies.

The JR density model requires a smoothed value of $F_{10.7}$, defined as the 81–day mean solar flux $\overline{F_{10.7}}$ centered at epoch. As such, the atmospheric density at the beginning of an orbit propagation interval depends equally on $F_{10.7}$ observations and predictions. As the orbit propagation proceeds $\overline{F_{10.7}}$ becomes increasingly dependent on predictions; after 40 days $\overline{F_{10.7}}$ depends entirely on predictions. The JR model also requires predicted daily values of K_p, but only to the end of the orbit prediction interval since the model does not require a smoothed value.

The SESC produces weekly a 27–day outlook of the daily $F_{10.7}$ solar flux, forecasting the periodic variation in $F_{10.7}$ expected during the next solar disk rotation. A regression algorithm[13] establishes a trend based on the past three solar rotations, weighted toward the most recent rotation. This long–term trend is compared with a more recent trend observed within the past two or three days. If the two trends are in opposite directions, the prediction follows the direction of the more recent trend, but then regresses toward the long–term trend. This technique assures that the beginning of each 27–day outlook transitions smoothly from the most recent daily observations. For prediction intervals longer than 27 days, the SESC also updates monthly a forecast of an average $F_{10.7}$ solar flux to the end of the current solar cycle, including an envelope of the expected ±90–percentile variations. The SESC Forecast Desk cautions that their outlook conveys expected trends, rather than rigorous predictions. While the outlook may often reflect analyst technique as much as procedure, we have assumed that all SESC outlook data are of equal quality.

To measure the SESC 27–day outlook performance, data have been organized into annual groups consisting of 52 weekly sets for direct comparison with *uncorrected* daily observations. The outlook data cover 1983–90 and are contained in SESC *PRFs* 400–799 (1983 includes only the last 36 weeks). Annual groups have been established to detect any trends which may be related to the solar cycle. At present the SESC does not provide daily $F_{10.7}$ predictions beyond 27 days that include effects periodic with solar disk rotation. To facilitate computation of $\overline{F_{10.7}}$, an 81–day prediction span has been constructed by repeating the SESC 27–day outlook three times.

Figs. 4(a,b) show the daily algebraic mean and absolute mean $F_{10.7}$ prediction errors over 81 days for each annual set. The algebraic mean errors (prediction minus observation) exhibit some bias for most years. In 1988 the outlook significantly underpredicted because solar activity increased at a much faster and sustained rate than expected (Figs. 1, 3a). In general, the annual absolute mean errors vary with the solar cycle reflected by the observed annual mean $F_{10.7}$ (Fig. 3b). Normalizing the absolute mean $F_{10.7}$ prediction errors for each year by the corresponding observed annual $F_{10.7}$ standard deviation removes this proportionality factor and provides a common basis for year–to–year comparisons. Fig. 4(c) shows the yearly normalized absolute mean errors ($\Delta F/\sigma_F$) are consistently grouped between 0.5 and 1.0, indicating the annual prediction accuracies are very similar.

The SESC $F_{10.7}$ outlook is significantly more accurate during the first 7–10 days, primarily because the predictions transition smoothly from recent observations. The higher accuracy at the beginning of the prediction span improves orbit propagation accuracy because the earliest $F_{10.7}$ errors act for the longest time. The $F_{10.7}$ errors during the second and third repetitions of the 27–day outlook are not significantly larger than earlier maximum errors, indicating a three–repetition strategy effectively facilitates computation of $\overline{F_{10.7}}$.

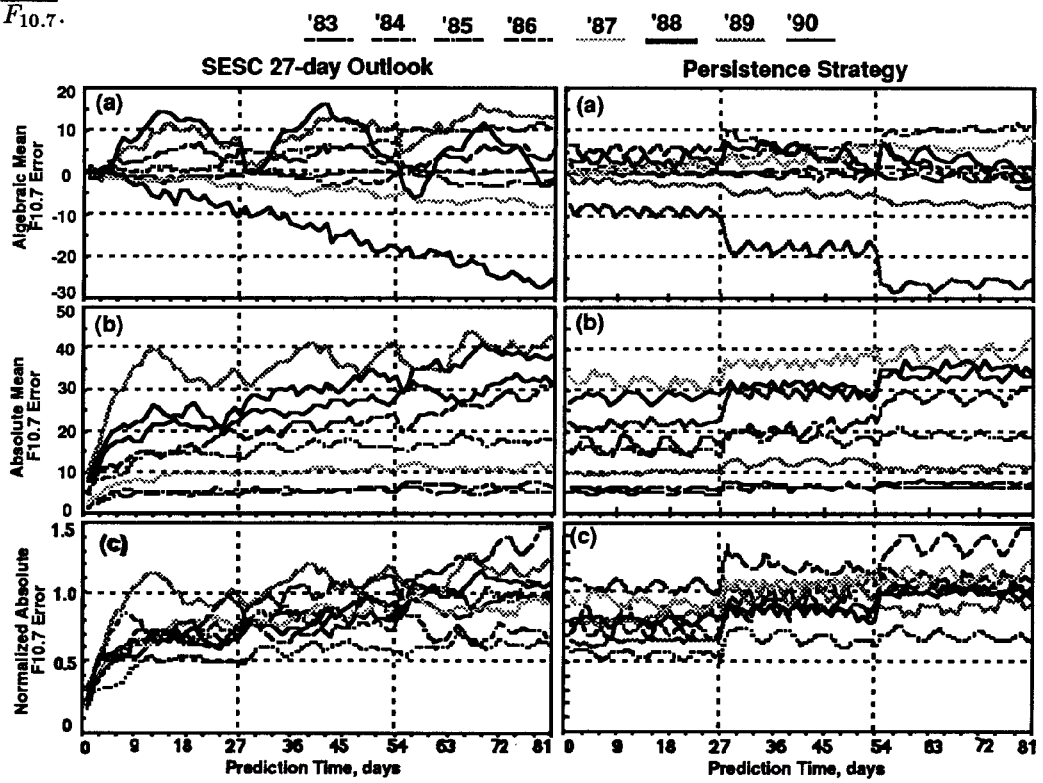

Fig. 4. Comparison of $F_{10.7}$ Prediction Accuracies for SESC 27–day Outlook and Simple Persistence Strategy (1983–90): (a) Algebraic Mean Error, (b) Absolute Mean Error, (c) Normalized Absolute Mean Error ($\Delta F/\sigma_F$).

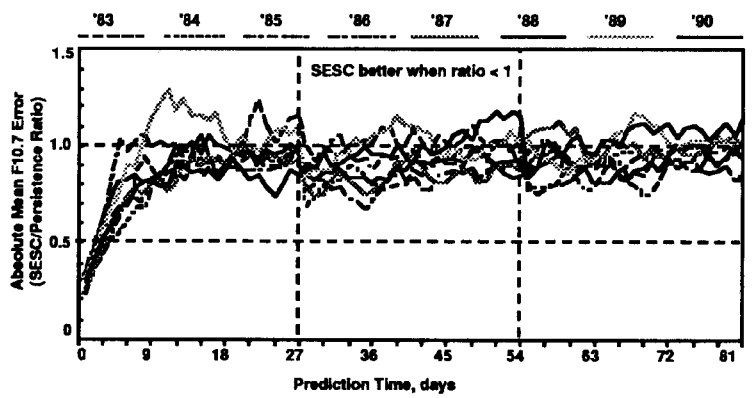

Fig. 5. Ratio of Absolute Mean $F_{10.7}$ Errors (SESC/Persistence).

We have attempted to "grade" the SESC 27–day outlook by direct comparison with an arbitrary forecast technique that assumes the most recent 27 daily observations repeat. Use of this simpler *persistence* strategy may be preferable if shown to be as accurate as the SESC outlook. The right side of Figs. 4(a–c) clearly indicates the persistence strategy generally exhibits larger algebraic and absolute mean $F_{10.7}$ errors over 81 days. However, the ratio of the absolute mean $F_{10.7}$ errors for the two prediction strategies (Fig. 5) shows that the SESC outlook performs better overall, especially during the first 7–10 days.

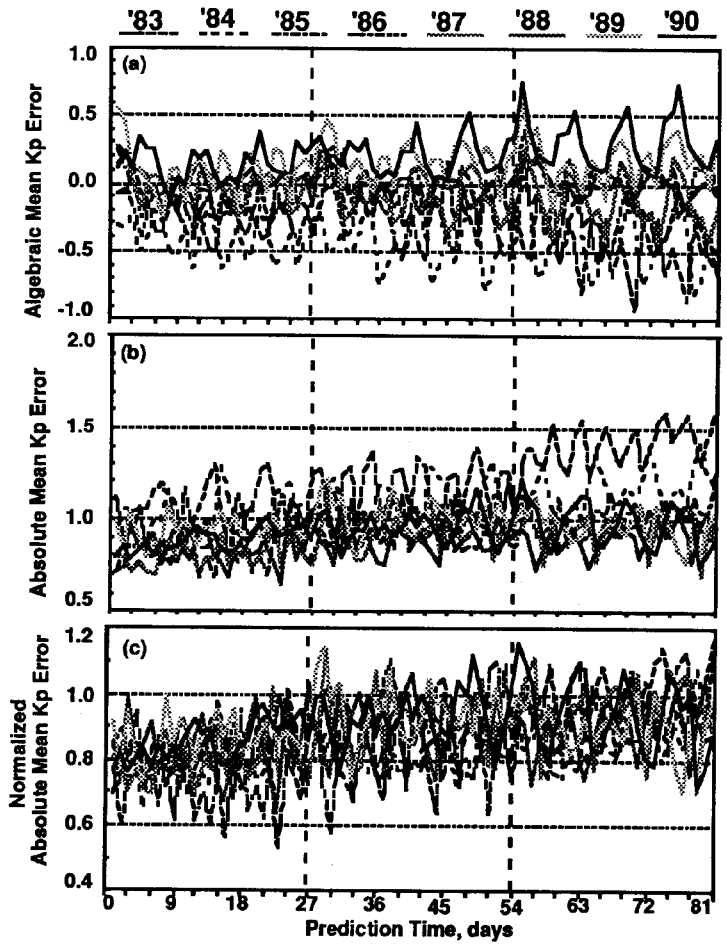

Fig. 6. Accuracy of SESC 27–day Outlook of Geomagnetic Index K_p (1983–1990): (a) Algebraic Mean Error, (b) Absolute Mean Error, (c) Normalized Absolute Mean Error ($\Delta K_p/\sigma_{K_p}$).

Geomagnetic Index Predictions

The SESC also provides the 27–day outlook for A_p in weekly *PRFs*; like the $F_{10.7}$ outlook, these data also transition smoothly from recent daily observations. Observed data (Figs. 2,3) show similar geomagnetic activity levels from year–to–year, being slightly higher and more variable during the declining years of the cycle when geomagnetic storms are more prominent. The primary challenge then becomes predicting sudden increases which can result from flares and/or recurrent coronal hole disturbances.

Since the JR density model uses K_p, both the A_p observations and SESC outlook values are converted to equivalent K_p values for comparison. We have used a conversion that preserves the exospheric temperature correction[11] due to geomagnetic heating defined by the JR density model: $\Delta T_\infty = A_p + 100[1 - e^{-0.08A_p}] = 28K_p + 0.03e^{K_p}$ (Eq. 2). For TOPEX/POSEIDON, K_p round-off to the nearest 0.1 was determined as sufficient.

The K_p outlook has been extended to 81 days using three repetitions of the 27-day outlook as was also done for the $F_{10.7}$ outlook. The algebraic mean K_p errors shown in Fig. 6(a) exhibit only moderate biases for most years, generally ranging between ± 0.5. The period of greatest underprediction for the SESC outlook occurred in 1983 and 1984 during the solar cycle decline, indicating the higher activity level was not reflected in the outlook. The largest overprediction occurred in 1990 following solar maxima.

The absolute mean K_p prediction error shown in Fig. 6(b) averages about 1.0 for most years, a level equal to about one standard deviation (see Fig. 3c). However, the normalized absolute mean error shown in Fig. 6(c) is well below 1.0 at the beginning of the prediction period, exhibiting gradual linear growth over 81 days. This behavior is evident for every year in this database, suggesting additional loss in accuracy for longer prediction periods.

GROUND TRACK PREDICTIONS

Ground track prediction errors include uncertainties in maneuver execution, orbit determination, and drag computation. Maneuver execution errors arise from incomplete knowledge of thruster efficiencies and ΔV pointing errors, especially early in the mission. Thrust magnitude errors are expected to be less than 1.5% (3σ), while the expected fixed magnitude error is 0.4 mm/s (3σ); the maneuver ΔV pointing error is expected to be less than 4.5° (3σ) using active attitude control.[18] The ground track prediction error allocated to orbit determination is 225 meters (3σ) of equatorial longitude after 30 days, equivalent to an initial semi-major axis error of about one meter. Drag computation errors arise from systematic density modelling errors ($\sim$15%, 1σ),[12] inaccurate area and C_d modelling, and errors in predicting solar and geomagnetic activity.

The effects of $F_{10.7}$ and K_p prediction errors on the ground track were examined for each of the two strategies described earlier: a three-cycle repetition of the SESC outlook, and a three-cycle repetition of the most recent 27 daily observations. Ground tracks were generated for the same weekly intervals from 1983 to '90, and grouped into yearly sets for analysis. Each ground track was calculated for 81 days using the mean element propagator[2] with a 17×17 geopotential, lunar-solar gravity, the simplified density model, the VMA model, and a four-orbit integration step size. The initial vector for each propagation was positioned at the east boundary of the ± 1-km bandwidth, phased to have the appropriate current nodal-plane orientation (Ω). As a baseline for comparison, corresponding "actual" ground tracks were generated using observed values of $F_{10.7}$ and K_p.

Figure 7 compares the algebraic mean ground track prediction error μ for each annual set after 27 days, and after 81 days. Positive values of μ indicate higher than expected drag, resulting in an eastward drift relative to the actual ground track; negative μ values indicate the exact opposite. Higher predicted drag results from overpredicting $F_{10.7}$ and/or K_p ; lower drag results from underpredicting either of these parameters. During periods of lower solar flux (from 1984 through '88), $\mu_{SESC} < 0$ occurred consistently; whereas $\mu_{SESC} > 0$ occurred during years of higher solar flux (1983, '89, '90). However, these definite trends are not evident for the persistence strategy; in fact, $\mu_{persistence} > 0$ occurred for most years (1983, '84, '86, '89, '90).

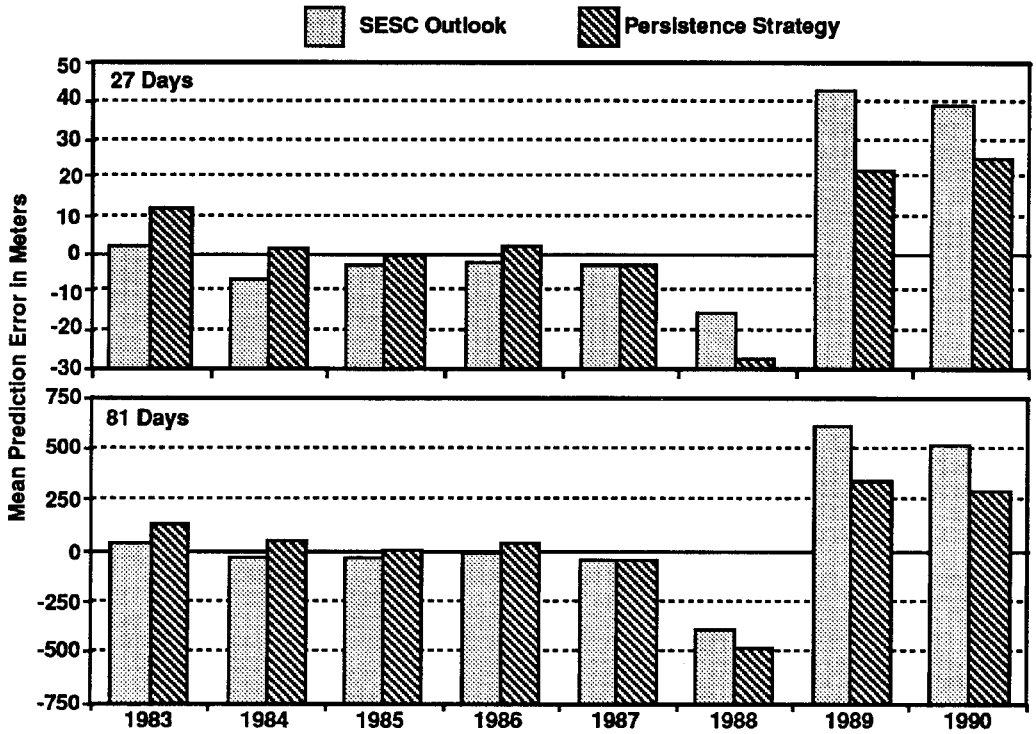

Fig. 7. Ground Track Prediction Errors due to Solar Activity Prediction Errors.

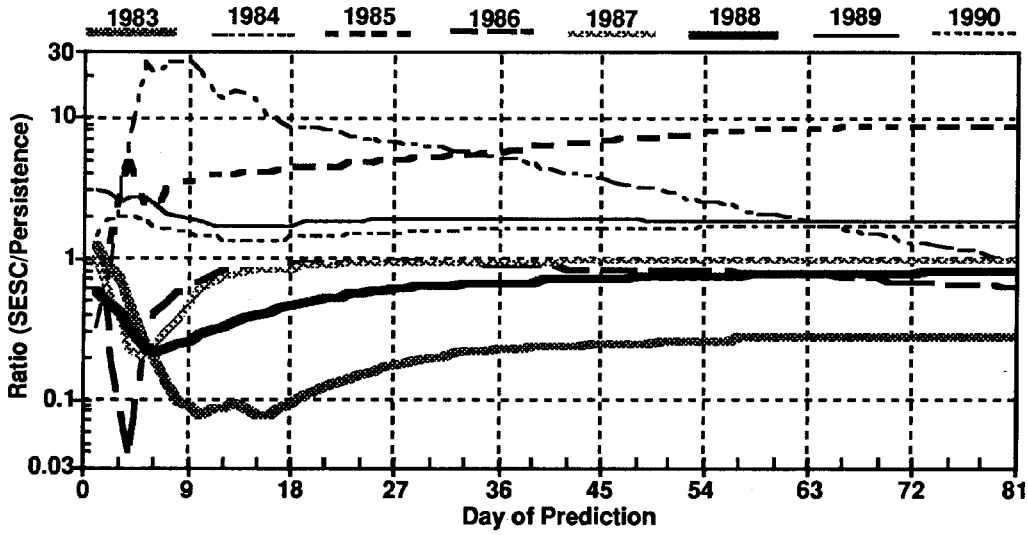

Fig. 8. Ratio of Absolute Mean Ground Track Errors.

For this ground track targeting problem, under–predicting drag is generally safer, because it merely causes the ground track to turn eastward sooner. Over–prediction of drag leads to selection of a larger than necessary maneuver, requiring another maneuver to reverse the ground track and prevent crossing the western boundary.

The ratio $r = \left|\frac{\mu(SESC)}{\mu(persistence)}\right|$, shown in Fig. 8, provides a direct comparison of the error magnitudes between the two prediction techniques. When $r < 1$ the SESC outlook predicted the ground track more accurately. This occurred in 1983, '86, '87, and '88, all years of higher solar activity (except '86). In the other years between 1983–90 $r > 1$, suggesting that persistence was more accurate during these years. The data for 1983 through 1987 provide the most valid comparison for the TOPEX/POSEIDON mission, as these data cover a similiar region of the solar cycle (see Fig. 1). During three of these years (1983, '86, '87) $r < 1$. Although $r > 1$ during 1984 and '85 indicates that persistence was more accurate relative to the SESC outlook, the actual biases themselves were small (less than 10 meters in ground track after 27 days). The larger positive ground track biases for the SESC outlook in 1989 and '90 indicate an eastward error resulting from over–predicting drag (e.g., over–predicting $F_{10.7}$). The reason for the smaller biases for the persistence strategy during 1989 and 1990 is not yet clear.

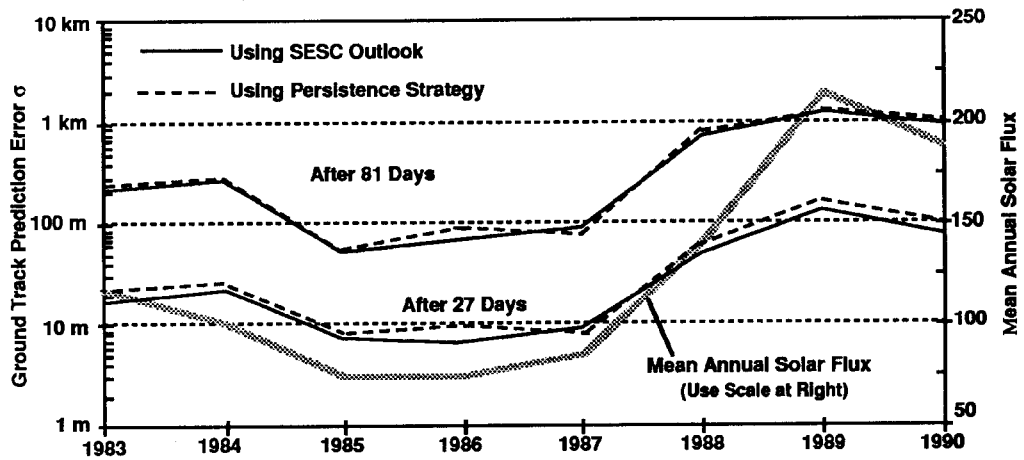

Fig. 9. Variations in Ground Track Error due to Solar Activity Prediction Errors.

While the evidence supporting the superiority of the SESC outlook is not overwhelming when measured in terms of mean ground track error, the standard deviation (σ) is more conclusive (Fig. 9). In all years except 1987, the ground track errors exhibit a tighter distribution about the algebraic mean (bias). The trend in the error magnitudes is similar in shape to the annual variations in $F_{10.7}$, peaking with the solar maximum. The earlier years correspond more closely to the phase of the solar cycle during which the TOPEX/POSEIDON mission will occur. During these years use of the SESC outlook predicted smaller overall ground track errors with a tighter distribution than predicted by persistence. Thus the remainder of this paper concentrates on the use of the SESC outlook for generating ground track biases for use in maneuver design.

The growth in the standard deviation (σ) and worst case ($\pm$100–percentile) ground track errors for predictions using the SESC outlook are shown in Fig. 10. Both grow as $\sim t^n$, where $n \simeq 2$. The lines in Fig. 10 can be extrapolated as necessary to obtain targeting

biases corresponding to a 95% confidence level. An unbiased prediction with a normal error distribution contains 95% of the errors within $\mu \pm 1.645\sigma$. The most conservative approach uses an interpolation of the ± 100 percentile curves. A less conservative approach treats the errors as unbiased and normally distributed and extrapolates the appropriate σ curve.

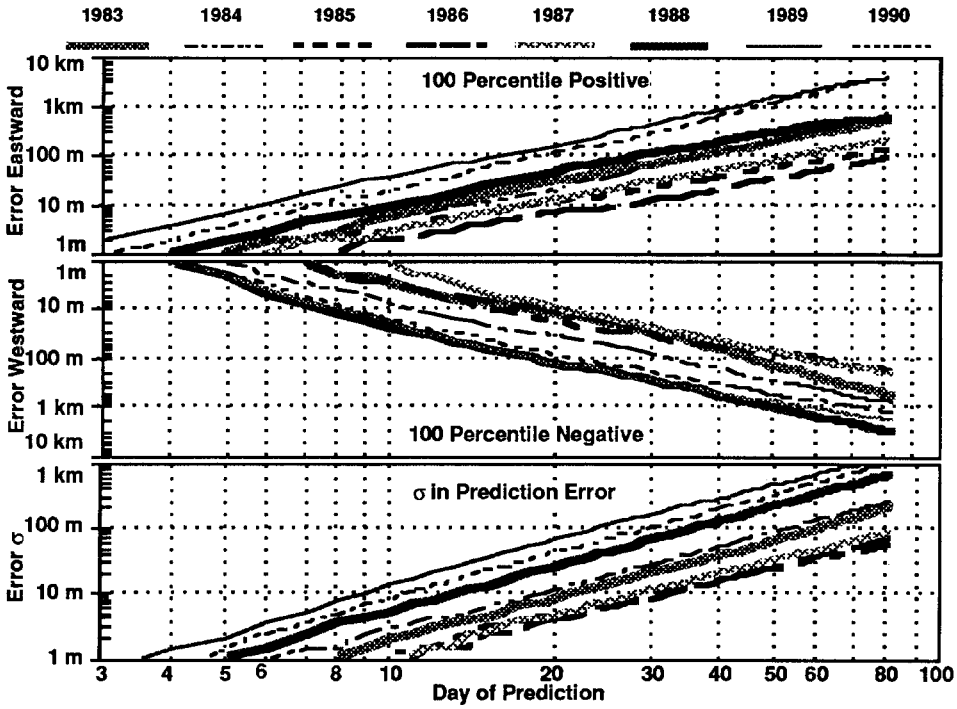

Fig. 10. Worst Case (100–percentile) and Standard Deviation (σ) in Ground Track Prediction Using SESC Outlook.

ORBIT MAINTENANCE MANEUVER DESIGN

Two different targeting strategies can be used for orbit maintenance: *longitude targeting* and *time targeting*, as shown in Fig. 11. *Longitude targeting* utilizes the full 2–km bandwidth to maximize the time between maneuvers. When the ground track is at the eastern boundary, a maximum magnitude maneuver ΔV_{max} is applied to increase the semi–major axis. The resulting higher nodal period causes the ground track to drift westward from the eastern boundary. Drag continuously reduces the nodal period until the ground track becomes just tangent to the western boundary; the ground track then reverses eastward as the period continues to decrease, eventually returning to the eastern boundary at a time T_{max}. When the eastern boundary is reached, the next maintenance maneuver is applied utilizing another *longitude targeting* sequence. Had a larger maneuver $\Delta V > \Delta V_{max}$ been applied, the ground track would have crossed the western boundary prior to turning around; a maneuver smaller than ΔV_{max} causes the ground track to return sooner to the eastern boundary. In either case, the next maneuver occurs sooner than planned. In *time targeting*, the maneuver spacing T is selected, and a maneuver ΔV is applied so that the next ground track returns to the eastern boundary after time T. For *time targeting*, $\Delta V < \Delta V_{max}$ and $T < T_{max}$.

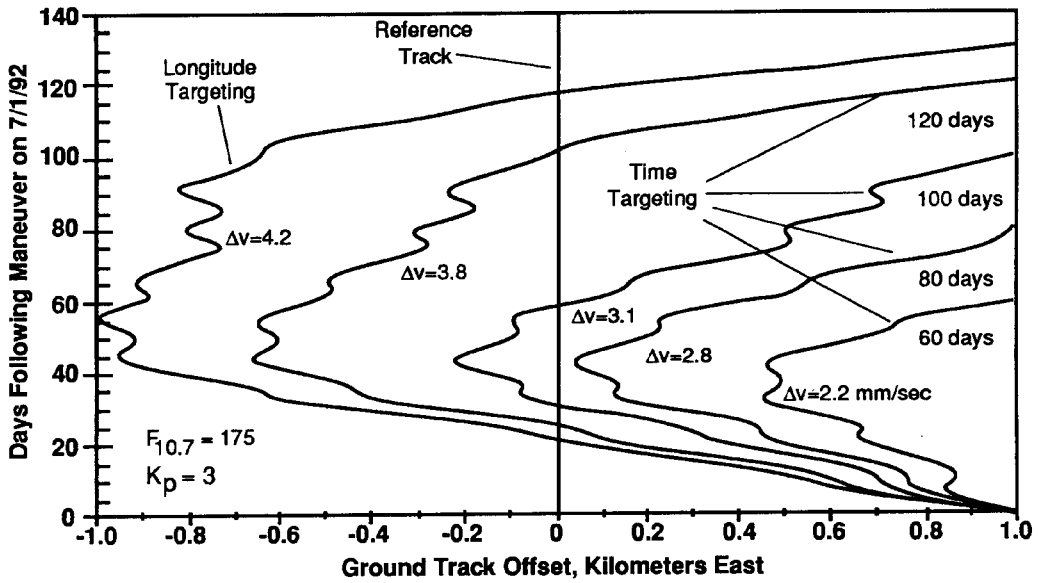

Fig. 11. Comparison of Longitude and Time Targeting Strategies.

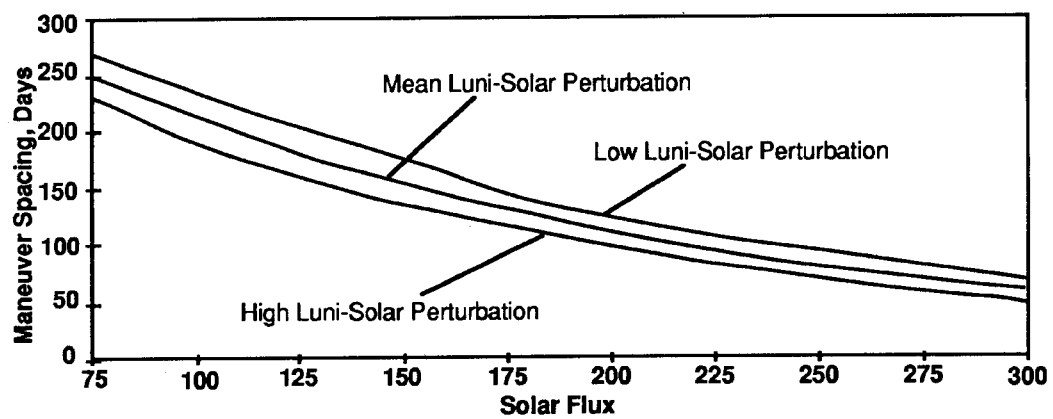

Fig. 12. Variations in Expected Maneuver Spacing due to Luni–Solar Gravity and Solar Flux($K_p = 3$).

Figure 12 expresses the maneuver spacing in terms of $F_{10.7}$ for constant $K_p = 3$. The middle curve shows the expected spacing using *longitude targeting* in the presence of average lunar–solar perturbations. The two outer curves bound variations in maneuver spacing for deterministic extremes in lunar–solar orientation during the first two years of the TOPEX/POSEIDON mission. In this example, additional variations result from unpredicted changes in $F_{10.7}$, and deviations from $K_p = 3$. Higher values of either $F_{10.7}$ or K_p reduce the resulting maneuver spacing; the effect is greatest when the increases occur soon after a maneuver. The spacing is further reduced by constraining maneuver placement between 10–day repeat cycles, and by biasing the ground track to contain expected orbit prediction errors within the 2–km control band.

The primary targeting objective is to determine a maneuver magnitude which contains

the ground track within the 2–km band 95% of the time, including the effects of orbit determination uncertainties, maneuver execution errors, and errors in predicting changes in $F_{10.7}$ and K_p. Using an iterative targeting algorithm, a ground track is first generated for an in–plane maneuver ΔV without prediction errors. This process uses mean element propagation[2] with all perturbations active and drag based on multiple repetitions† of the SESC 27–day outlook. For *longitude targeting* [2]

$$\Delta V = \sqrt{\frac{C_D A}{M} \frac{\rho V^3}{3} \frac{\Delta\lambda}{\omega_e}} \tag{8}$$

where $\Delta\lambda$ is the desired change in the ground track equatorial longitude, and ω_e is the earth rotation rate. For *time targeting*, the initial constant–drag approximation is

$$\Delta V = \frac{\rho A C_D V^2 T}{4M} \tag{9}$$

where T is the target time. The error–free ground track is stored as an array of equatorial ground track offsets $\Delta\lambda(t_i)$. The 95% error envelope is calculated as $e_i = \Delta\lambda(t_i) \pm \hat{\sigma}(t_i)$, where

$$\hat{\sigma}(t_i) = 1.645\sqrt{\sigma^2_{\Delta V}(t_i) + \sigma^2_{OD}(t_i) + \sigma^2_{Drag}(t_i)}. \tag{10}$$

Maneuver execution errors can be characterized in terms of their fixed and proportional components, combining as $\sigma^2_{\Delta V} = \sigma^2_{\Delta V_f} + \sigma^2_{\Delta V_p}$. For TOPEX/POSEIDON,[2] $\sigma_{\Delta V_f} \simeq 0.133$ mm/sec and $\sigma_{\Delta V_p} \simeq 0.005\Delta V$. The total ground track error due to $\sigma_{\Delta V}$ grows linearly with time,[2]

$$\frac{\partial\Delta\lambda}{\partial\Delta V} = -\frac{3\omega_e t}{V} \simeq -16.96t(days)\frac{meters}{mm/sec}. \tag{11}$$

Orbit determination errors, expressed here in terms of errors in the pre–maneuver semi–major axis Δa, introduce a design error in the nominal maneuver ΔV. For a circular orbit, this velocity error $dV \simeq -(V/2a)/\Delta a$. Substitution of dV into Eq. (11) expresses the linear growth in the ground track error in terms of Δa.

$$\frac{\partial\Delta\lambda}{\partial a} \simeq \frac{3}{2}\frac{\omega_e}{a}t \simeq 7.81t(days)\frac{meters}{meter}. \tag{12}$$

Errors in semi–major axis due to orbit determination are expected to be $\sigma_a \simeq 0.33$ meters ($dV \simeq 0.155$ mm/sec), corresponding to a 3σ ground track prediction error of $\sim$234 meters after 30 days.

Equation (10) assumes that the three error sources are independent and normally distributed. *Longitude targeting* determines the ΔV to contain the worst case e_i just inside the western boundary. Successive linear differential corrections are applied to reduce the western–most e_i to the desired level (e.g., $\sim$10 meters). Targeting may also be accomplished by selecting the ΔV to minimize e_i within an acceptable fixed error limit ($\sim$ 0.133 mm/sec, 1σ). Increased convergence speed may be possible using the quadratic dependence of $\Delta\lambda$ on ΔV (Eq. 8), but this technique ignores drag fluctuations and luni–solar perturbations. For *time targeting*, successive ΔV iterations limit the error in the achieved value of T, which can be targeted for either the western or eastern boundaries.[2]

† The number of repetitions must be carefully chosen to avoid divergence from expected $\overline{F_{10.7}}$ trends (e.g., downward in declining years of the solar cycle).

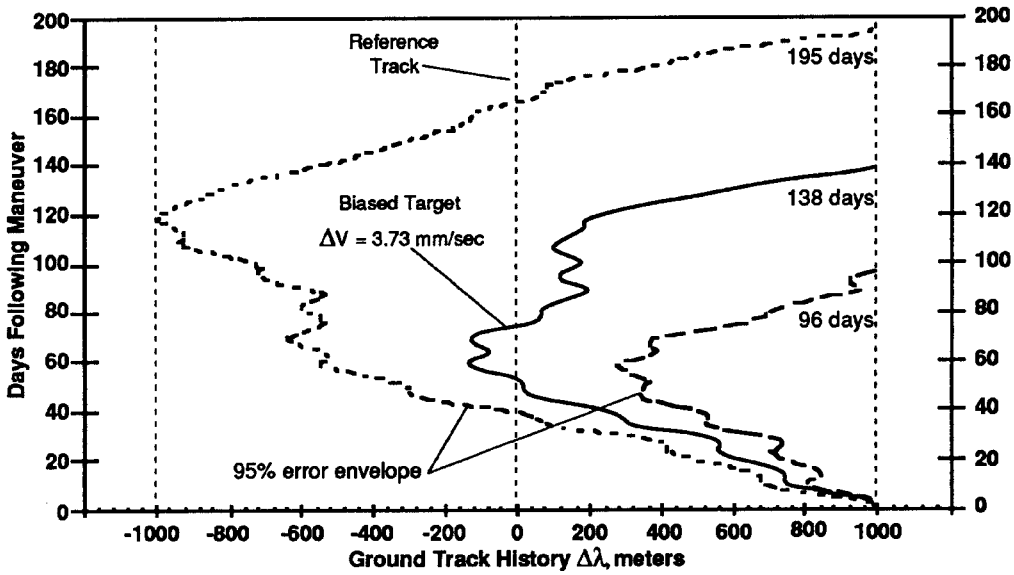

Fig. 13. Longitude Targeting Strategy using Ground Track Biases for Solar Activity Prediction Errors (Sample Year 1984).

Figure 13 illustrates this algorithm for *longitude targeting* initiated from the eastern boundary. An epoch of 1 June 1984 was chosen to utilize a solar activity profile similar in form to that expected during the second or third year of the TOPEX/POSEIDON mission. This period covers the solar cycle decline when the observed annual mean $F_{10.7}$ was ~101 (Fig. 3a). The SESC 27-day outlook was repeated for the duration of the prediction interval. Required ground track biasing incorporates the prediction errors due to drag, orbit determination, and maneuver execution. The drag contribution to $\hat{\sigma}$ was obtained by extrapolating the 1984 σ curve in Fig. 10. For this example, the biased target required a ΔV of ~ 3.73 mm/sec; the ground track returned to the eastern boundary after 138 days. The ±95% error envelopes (Eq. 10) returned after 195 days and 96 days, respectively. The later time occurs if *a)* the drag experienced was lower than expected, *b)* a larger ΔV than desired was performed, and/or *c)* the pre-maneuver semi-major axis was larger than estimated by orbit determination. The earlier time occurs when these error conditions are reversed.

For comparison, an unbiased ΔV was also targeted (not shown). This strategy required a $\Delta V \simeq 4.34$ mm/sec and returned to the eastern boundary after 200 days. Thus the maneuver bias was $\delta(\Delta V) \simeq 0.61$ mm/sec, nearly all due to errors in predicting solar activity (~0.51 mm/sec). This ΔV bias is ~14% of the unbiased value, and the subsequent maneuver time is ~30% earlier.

This example illustrates the significant ΔV bias which must be applied to account for ground track prediction errors. For $\overline{F_{10.7}}$ levels greater than 100, the ΔV bias will be larger. The bias is expected to be smallest near the solar minima when the mimimum maneuver ΔV will be required. The character of the maneuver design then shifts as the fixed maneuver velocity error and the orbit determination uncertainty emerge as the dominant contributors to a ΔV bias. During this portion of the mission repeated *time targeting* maneuvers may be used to "ping-pong" back and forth between the eastern and western boundaries.[2]

SUMMARY

The SESC 27–day outlook of $F_{10.7}$ and A_p has been shown to be more accurate than a simpler persistence strategy that arbitrarily assumes an exact repeat of the most recent 27 daily observations. This superiority is most pronounced during the first 7–10 days because the SESC outlook is constrained to transition smoothly from recent observations, whereas the persistence strategy is not. The SESC outlook tends to exhibit higher $F_{10.7}$ prediction errors during periods of high solar activity, but these errors do not increase significantly across three repetitions of the 27–day outlook. Prediction errors for the SESC 27–day outlook for K_p are somewhat larger during the declining years of the solar cycle, with modest error increases during the second and third 27–day repetitions.

Comparisons of ground track prediction errors indicate use of the SESC outlook under–predicted drag during low solar flux (1984–88), while over–prediction was evident in 1983, 1989, and 1990. Use of persistence to forecast drag did not demonstrate a clear trend although it did out–perform the SESC outlook in some years. Overall the SESC outlook is preferable to the persistence strategy because it consistently demonstrates higher accuracy during the first 7–10 days.

The targeting example using solar activity from 1984 indicates the need for a significant maneuver ΔV bias to account for expected orbit prediction errors, nearly all of which were attributed to errors in predicting changes in solar activity. At the solar minima, orbit determination and maneuver execution errors are expected to dominate, thereby reducing overall ground track controllability. New strategies using ΔVs of only a few millimeters/sec may become necessary.

More work is needed to better determine the appropriate number of repetitions of the SESC outlook to be applied in a targeting process. This becomes particularly important when the solar flux level is expected to change considerably during the targeting interval, as would be expected during solar cycle decline. It may be more appropriate to determine ground track biasing from data sets shorter than the one–year period selected in this study.

ACKNOWLEDGEMENT

The authors wish to acknowledge that Eric Cannell developed an earlier version of the simplified density model; the authors have added the orbital averaging and the annual and semi–annual variations.

REFERENCES

1. Tapley, B. D., "Orbit Determination Requirements for TOPEX,"AAS/AIAA Astrodynamics Specialist Conference, August 1987, Kalispell, Montana, AAS–87–429.
2. Bhat, R. S., Frauenholz, R. B., Cannell, P. E.,"TOPEX/POSEIDON Orbit Maintenance Maneuver Design, " AAS 89–408, 1989 AAS/AIAA Astrodynamics Specialist Conference, Stowe, Vt., August 1989.
3. Marsh, J.G., et al, "The GEM–T2 Gravitational Model," NASA Technical Memorandum 100746, October 1989.
4. Vincent, M. A., "The Inclusion of Higher Degree and Order Gravity Terms in the Design of a Repeat Ground Track Orbit," AIAA 90–2899–CP, 1990 AIAA/AAS Astrodynamics Conference, Portland, Or., August 1990.
5. Guinn, J. R., "Short Period Gravitational Perturbations for Conversion Between Osculating and Mean Orbit Elements," AAS 91–430, 1991 AAS/AIAA Astrodynamics Specialist Conference, Durango, Co., August 1991.
6. Escobal, P. R., *"Methods of Astrodynamics,"* Robert E. Kreiger Publishing Company, Inc., Huntington, New York, 1979.
7. Jacchia, L. G., *Static Diffusion Models of the Upper Atmosphere with Empirical Temperature Profiles*, Smithsonian Astrophysical Observatory Special Report 170, 30 December 1964.
8. Jacchia, L. G., " Atmospheric Models in the Region From 110 to 2000 km," in *CIRA–72: COSPAR International Reference Atmosphere 1972*, ed. The Committee for the COSPAR International; Reference Atmosphere (CIRA) of COSPAR (Committee on Space Research) Working Group 4, Akadamie–Verlag, Berlin, 1972.
9. Jacchia, L. G., *Thermospheric Temperature, Density, and Composition: New Models*, Smithsonian Astrophysical Observatory Special Report 375, 15 March 1977.
10. Roberts, Charles, "An Analytic Model for Upper Atmosphere Densities Based Upon Jacchia's 1970 Models", *Celestial Mechanics*, 4(1971), 368–377.
11. Cappellari, J.O., Velez, C.E., and Fuchs, A.J., ed., *Mathematical Theory of the Goddard Trajectory Determination System*, Goddard Space Flight Center X–582–76–77, April 1976.
12. Marcos, Frank A., Killeen, Timothy L., Roble, Raymond G., "Evaluation of New Atmospheric Drag Modeling Techniques," AAS 89–419, 1989 AAS/AIAA Astrodynamics Specialist Conference, Stowe, Vt., August 1989.
13. Nostrand, Philip, M., "Forecast Verification of the 10.7 Centimeter Solar Flux and the A_p Daily Geomagnetic Activity Indices," Report No. AD–A152959, Department of the Air Force, Air Force Institute of Technology, Wright–Patterson Air Force Base, Ohio, December 1984.
14. Withbroe, George, L., "Expectations for Solar Activity in the 1990's," AAS 89–417, 1989 AAS/AIAA Astrodynamics Specialist Conference, Stowe, Vt., August 1989.
15. McCormac, F.G., Killeen, T.L., Burns, A.G., Marcos, F.A., and Roble, R.G., "The Effect of Solar Cycle Variations on the Thermosphere," AAS 89–416, 1989 AAS/AIAA Astrodynamics Specialist Conference, Stowe, Vt., August 1989.
16. Heckman, Gary R., "Predictions of the Space Environment Services Center," *Solar–Terrestrial Predictions Proceedings, Vol. 1*," edited by R. F. Donnelly: 322–349. Boulder, Co., December 1979.
17. Joselyn, Jo Ann, "Case Study of the Great Geomagnetic Storm of 13 March 1989," AAS 89–418, 1989 AAS/AIAA Astrodynamics Specialist Conference, Stowe, Vt., August 1989.
18. Bhat, R. S., "TOPEX/POSEIDON Orbit Acquisition Maneuver Design," AAS 91–514, 1991 AAS/AIAA Astrodynamics Specialist Conference, Durango, Co., August 1991.